Composite Structures 96 (2013) 745–750

Contents lists available at SciVerse ScienceDirect

Composite Structures

journal homepage: www.elsevier.com/locate/compstruct

Modeling microscale instabilities in compressed carbon nanotube bundles using multistable spring models

F. Fraternali [a,*], J.R. Raney [b], C. Daraio [b]

[a] Department of Civil Engineering, University of Salerno, 84084 Fisciano, SA, Italy
[b] Engineering and Applied Science, California Institute of Technology, Pasadena, CA 91125, USA

ARTICLE INFO

Article history:
Available online 8 October 2012

Keywords:
Carbon nanotube pillars
Multistable springs
Microscopic instabilities
Parameter identification

ABSTRACT

We formulate *in situ* parameter identification techniques for multistable spring models of compressed CNT bundles, which capture the sequential buckling through the height of the bundle, as well as the overall mechanical response. The proposed techniques are validated against a SEM-assisted compression experiment on a CNT pillar [1]. Using multi-spring models, we propose a 'microscopic' identification technique based on the determination of stress–strain curves of vertical segments of the tested structure (featuring few micron height). We show that the *in situ* identified models can effectively reproduce the experimentally-observed stress–strain response (single-spring models), and strain localization effects (multi-spring model), within a simple 1D framework.

1. Introduction

Carbon nanotubes (CNTs) have been of great interest for a variety of applications due to their excellent mechanical, electrical, and thermal properties, and the low density of structures of CNTs [2]. They can be readily synthesized using simple chemical vapor deposition techniques into low-density structures of nominally-aligned CNTs (e.g., [3]). These structures can exhibit foam-like properties in compression [4] as well as interesting strain localization and collective buckling effects [5]. Aligned arrays of CNTs have the potential to be used as stand-alone multifunctional, low-density energy-dissipative materials (e.g., [4,6]), or as components in advanced composites leading to enhanced electrical [7], multifunctional [8], and mechanical [9,10] properties relative to traditional composites. These potential applications have motivated efforts to understand the details of the mechanical response and the mechanisms involved with the behavior of the systems. In compression, a hysteretic stress–strain response is observed, which in the past has been related to the behavior of open cell foams [4,11]. Depending on synthesis conditions, CNT arrays have been observed to either recover most of their original height after compression (e.g., [4,12]) or to stay completely collapsed (e.g., [1,5]), with some evidence for switching between these behaviors [13].

Photolithographic techniques have been used in the past to synthesize various patterns of CNT structures (e.g., [14]), such as microscale pillars [1,15]. These (order 10–100 μm diameter) pillars have proven ideal for experimentally visualizing, e.g., via *in situ* scanning electron microscopy (SEM), microscale deformation of these compliant structures. In particular, *in situ* videos during compression of pillars show local rearrangements of CNTs and the formation of collective buckles to accommodate increasing compressive strain [1]. These form sequentially from the base upward, with each buckle completing prior to the formation of a new buckle, and with the upper part of the structure (the part not involved with buckling) undergoing only a minimal fraction of the overall deformation. It has also been noted that the stress–strain response of compressed CNT bundles typically features repeated stress-drops with increasing compressive strain. Each drop takes place simultaneously to the nucleation or the propagation of a buckle [1,15]. Discontinuous stress drop phenomena are less frequent in compression experiments of much larger, millimeter-scale CNT arrays, since the dominant mechanics at the mesoscale often masks the microscale instabilities associated with the progressive buckling of the tubes, by averaging the local deformation over a larger length scale (cf., e.g, [4,6]).

Some recent studies acknowledge a temperature- and rate-independent character to the dissipative behavior of CNTs [16,17], arguing that the energy dissipation properties of such structures mainly originate from dynamic snap events due to attachments/detachments of individual tubes, driven by van der Waals forces [16], and/or local kinking of portions of the tubes [17]. These snaps occur over an internal timescale much faster than the external loading, giving rise to mesoscopic and macroscopic time-independency of the material response. It is also worth noting that fatigue-type damage (material preconditioning) of compressed CNT arrays has been observed with features similar to

* Corresponding author.
E-mail addresses: f.fraternali@unisa.it (F. Fraternali), raney@caltech.edu (J.R. Raney), daraio@caltech.edu (C. Daraio).

0263-8223/$ - see front matter © 2012 Elsevier Ltd. All rights reserved.
http://dx.doi.org/10.1016/j.compstruct.2012.09.013

the well known *Mullins effect* of filled rubbers and rubber-like materials [18]. Length-scale effects are magnified by inhomogeneity of material density and tubes' alignment along the thickness of CNT arrays, which typically feature higher density at the top of the structure (cf., e.g., [1,4,19]). The compression experiments on CNT pillars presented in [1] reveal that the buckling wavelength does not dependent on the applied strain-rate. In contrast, a more recent study [20] observes some influence of rate effects on the recovery and dissipation capacities of vertically aligned CNT pillars.

Multiscale models based on bistable spring elements have been recently proposed to capture the behavior of CNT arrays in compression, preconditioning damage, and the coupling of micro-, meso- and macro-scopic length scales [17,18]. Some of the main features of such models are the following:

- the modeling of stress drop events as *elastic phase transformations*, which mark fast, unstable transitions from the initial stress–strain regime (low or moderately large strains) to the local post-buckling response (material densification) of suitable elements of the structure (e.g., microscopic portions undergoing local buckling, elements of coarse-grained models, or the entire array, cf. [17]);
- the description of the material response at the meso- and macro-scales through *rate-independent hysteretlc models* [17,21];
- the inclusion of *fatigue-type damage* by setting to zero the stiffness of suitable springs [18];
- the possibility to model rate effects by placing dashpot elements in series or in parallel with the bistable spring units.

In [22], an *in situ* technique has been devised to allow bistable spring models to be applied to experimental results on the compression of CNT arrays, requiring only a video (with sufficient resolution to capture the strain localization due to local buckling) that is synchronized with the global stress–strain response of the system. So far, the above technique has only been applied to millimeter-scale CNT arrays which were observed with optical devices, with sufficient resolution only to capture the relevant mechanics at the model's meso- and macro-scopic scales [22].

In this paper, we model the micro-scale deformation of CNT pillars examining *in situ* scanning electron microscope (SEM) images of buckle formation and stress–strain data provided in [1]. We analyze a compression experiment on a 50 μm diameter CNT pillar and ≈1.2 aspect ratio (≈61 μm undeformed height), which was compressed up to 50% axial strain within a SEM-assisted apparatus (cf. Section 2). We model the response of the system using different spring models that account for multiple phase transformations along the given loading history, generalizing the bistable spring model presented in [17] (Section 3). We make use of single bistable spring (SBS), single multistable spring (SMS), and multiple bistable spring (MBS) models (Section 4). The material properties of the SBS and SMS models (representing the pillar as a unique 1D spring) are identified by simply inspecting the overall stress–strain response of the pillar, while those of the MBS model (representing the pillar as a collection of 1D springs piled one over the other, with each spring describing either a buckle or the unbuckled portion of the pillar) are determined through a SEM-assisted ('microscopic') identification technique [22] (Section 4). All the examined models allow us to capture the overall stress–strain response of the examined CNT pillar. The SMS and MBS models are also capable of reproducing all the sequential stress drops observed in the experiment. In particular, the MBS model is able to simulate strain localization phenomena and the individual formation of buckles. In each case, we prove that it is possible to successfully identify the constitutive properties of effective spring models of compressed CNT bundles, once the experimental stress–strain response and strain localization data are available. We draw the main conclusions of the present study in Section 5.

2. Analyzed experiment

The CNTs modeled in this study were grown via thermal chemical vapor deposition, as discussed in [1]. CNT pillars were obtained using a pre-patterned catalyst deposited on growth substrates using standard photolithographic techniques. A custom instrument that combines an SEM image acquisition system and a manipulator capable of compression, allowed the authors in [1] to obtain simultaneous images of compression with stress–strain data.

We show in Fig. 1 graphical renderings of selected frames extracted from an *in situ* video of the analyzed experiment (see [1], Supporting online material). The snapshots in Fig. 1 illustrate the collapse of the six folds that progressively appeared during the loading phase along the height of the tested pillar (cf. also [1], Figs. 4 and 5), and were taken in correspondence with the right extremes of the regions labeled with 1, 2, 3, 4, 5r, 5l and 6 in the stress–strain plot shown in Fig. 2. Region 1 corresponds to the nucleation of the first buckle at the right of the pillar and its propagation to the left; region 2 marks the nucleation of the second buckle at the left and its propagation to the right; region 3 corresponds to nucleation of the third buckle at the center-right and its propagation to left and right; region 4 is associated with the nucleation of the fourth buckle at the center-right and its propagation to left and right; region 5r corresponds to the nucleation of the fifth buckle at the right; region 5l marks the propagation of the fifth buckle to the left; and region 6 corresponds to the nucleation of the sixth buckle at the right and its propagation to the left. For

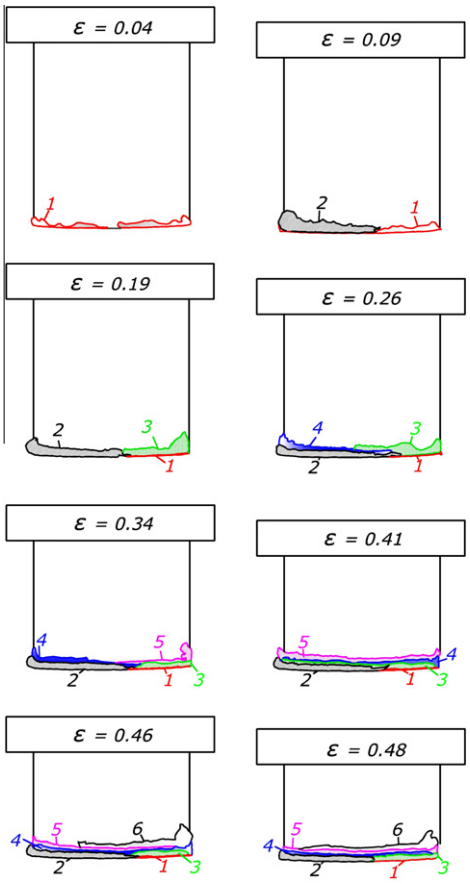

Fig. 1. Snapshots from the *in situ* video of the analyzed experiment showing the bottom-to-top succession of buckles observed via SEM [1].

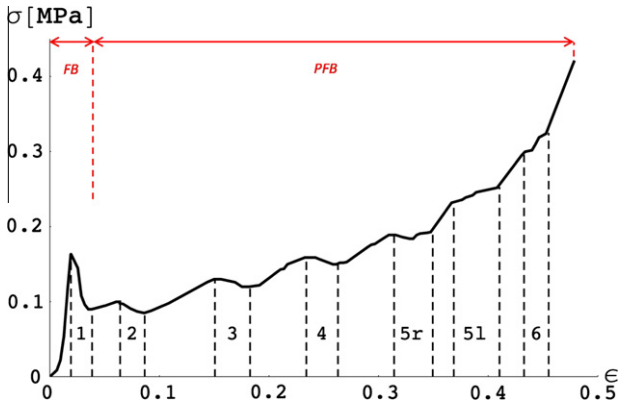

Fig. 2. Stress–strain response during the loading phase of the analyzed experiment. The labeled regions denote the snaps associated with the nucleation and collapse of the buckles shown in Fig. 1 (1: nucleation of the first buckle at the right of the pillar and its propagation to the left; 2: nucleation of the second buckle at the left and its propagation to the right; 3: nucleation of the third buckle at the center-right and its propagation to left and right; 4: nucleation of the fourth buckle at the center-right and its propagation to left and right; 5r: nucleation of the fifth buckle at the right; 5l: propagation of the fifth buckle to the left; 6: nucleation of the sixth buckle at the right and its propagation to the left).

future use, we let $\overline{P}_i^a = \left(\bar{\varepsilon}_a^{(i)}, \bar{\sigma}_a^{(i)}\right)$ denote the left-end point of region i and $\overline{P}_i^b = \left(\bar{\varepsilon}_b^{(i)}, \bar{\sigma}_b^{(i)}\right)$ the right-end point of same region, for i = 1, 2, 3, 4, 5*r*, 5*l*, 6. We also let $\overline{P}_7^a = \left(\bar{\varepsilon}_a^{(7)}, \bar{\sigma}_a^{(7)}\right)$ denote the end point of the stress–strain response in Fig. 2.

3. Mechanical modeling

We model the mechanical response of a CNT bundle through multistable spring elements featuring the stress–strain response $\sigma' - \varepsilon'$ shown in Fig. 3, where $\sigma' = \sigma - \sigma_0$, and $\varepsilon' = \varepsilon - \varepsilon_0$. Here and in what follows, σ and ε denote the actual stress and strain of the spring, respectively; σ_0 denotes an eventual prestress; and ε_0 denotes an eventual prestrain. The response shown in Fig. 3 alternates unstable phases (stress drops for increasing strains) and stable phases (stress increasing with strain). Eventually, two stable phases may follow each other without an intermediate unstable phase (say, e.g., the final densification phase and the unloading phase, cf. Fig. 3). Let (i) denote the region of the spring response formed by the succession of an unstable phase $\left(\sigma' = \sigma_{unst}^{(i)}\right)$ and the subsequent stable phase $\left(\sigma' = \sigma_{st}^{(i)}\right)$. We describe the corresponding stress–strain behavior through the equations

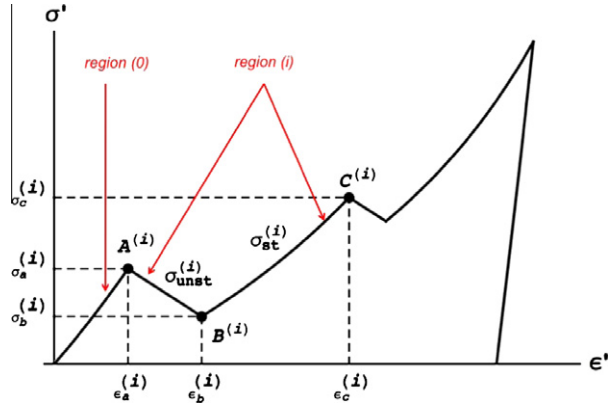

Fig. 3. Stress–strain response of a multistable spring model.

$$\sigma_{unst}^{(i)} = \sigma_a^{(i)} + \frac{\left(\sigma_b^{(i)} - \sigma_a^{(i)}\right)}{\left(\varepsilon_b^{(i)} - \varepsilon_a^{(i)}\right)}\varepsilon' \tag{1}$$

$$\sigma_{st}^{(i)} = \frac{k^{(i)}\left(\varepsilon' - \varepsilon_*^{(i)}\right)}{1 - \left(\varepsilon' - \varepsilon_*^{(i)}\right)} \tag{2}$$

where $\sigma_a^{(i)}$, $\sigma_b^{(i)}$, $\varepsilon_a^{(i)}$ and $\varepsilon_b^{(i)}$ are the quantities shown in Fig. 3, while $k^{(i)}$ and $\varepsilon_*^{(i)}$ are two additional constitutive parameters. It is seen that the unstable phases feature linear stress–strain response, while the stable phases feature a nonlinear stress–strain behavior ruled by the stiffness parameter $k^{(i)}$ and the strain parameter $\varepsilon_*^{(i)}$ (strain ε' at which the stress $\sigma' = \sigma_{st}^{(i)}$ is zero). The branch preceding region (1) in Fig. 3 describes the response of the spring when it is first loaded from the reference configuration $\varepsilon = \varepsilon_0$, $\sigma = \sigma_0$. We label (0) such a branch, which we model through the stress–strain relationship $\sigma' = \sigma^{(0)}$, where

$$\sigma^{(0)} = \frac{k_0\ \varepsilon'}{1 - \varepsilon'} \tag{3}$$

k_0 denoting an initial stiffness parameter. Under a given loading history, we determine the response of a system composed of one or more multistable springs (1)–(3) through the dynamic relaxation strategy illustrated in Section 4 of [17].

4. *In situ* parameter identification

4.1. SBS model

The first model we use to simulate the experiment described in Section 2 is composed of a single bistable spring, which features only regions (0) and (1) of the response illustrated in Fig. 3, and a total of five independent constitutive parameters, which we identify with k_0, $\varepsilon_a^{(1)}$, $\varepsilon_b^{(1)}$, $k^{(1)}$ and $\varepsilon_*^{(1)}$. By setting the prestrain ε_0 and the prestress σ_0 to zero, we let $\left(\varepsilon_a^{(1)}, \sigma_a^{(1)}\right)$ coincide with the coordinates $\left(\bar{\varepsilon}_a^{(1)}, \bar{\sigma}_a^{(1)}\right)$ of the first peak $\overline{P}_1^a$ of the experimental response. Next, we determine the initial stiffness k_0 by requiring that branch (0) passes through $\overline{P}_1^a$, obtaining

$$k_0 = \frac{\sigma_a^{(1)}\ \left(1 - \varepsilon_a^{(1)}\right)}{\varepsilon_a^{(1)}} \tag{4}$$

Regarding the stable portion of region (1), upon setting $\varepsilon_b^{(1)} = \bar{\varepsilon}_b^{(1)}$, we determine $k^{(1)}$ and $\varepsilon_*^{(1)}$ by fitting the function $\sigma_{st}^{(1)}$ defined by Eq. (2) to the portion $\overline{P}_1^b - \overline{P}_7^a$ of the experimental response in Fig. 2. Using the 'FindFit' function of *Mathematica*® 8, we obtain the set of constitutive parameters shown in Table 1, where $\sigma_b^{(1)}$ denotes the value attained by the best fit function $\sigma_{st}^{(1)}$ at $\varepsilon' = \varepsilon_b^{(1)}$. A comparison between the stress–strain response predicted by the SBS model and the experimental response is shown in Fig. 4.

4.2. SMS model

The second spring model analyzed in this work consists of a single spring featuring seven different 'post-buckling' regimes, hereafter denoted by the labels (1), (2), (3), (4), (5*r*), (5*l*), and (6), which follow the pre-buckling response (0). By setting the prestrain ε_0

Table 1
Constitutive parameters of the SBS model ($\varepsilon_0 = 0$; $\sigma_0 = 0$; initial stiffness: $k_0 = 8.357$ MPa).

Region	$\varepsilon_a^{(1)}$	$\sigma_a^{(1)}$ (MPa)	$\varepsilon_b^{(1)}$	$\sigma_b^{(1)}$ (MPa)	$k^{(1)}$ (MPa)	$\varepsilon_*^{(1)}$
1–6	0.019	0.164	0.038	0.058	0.1318	−0.269

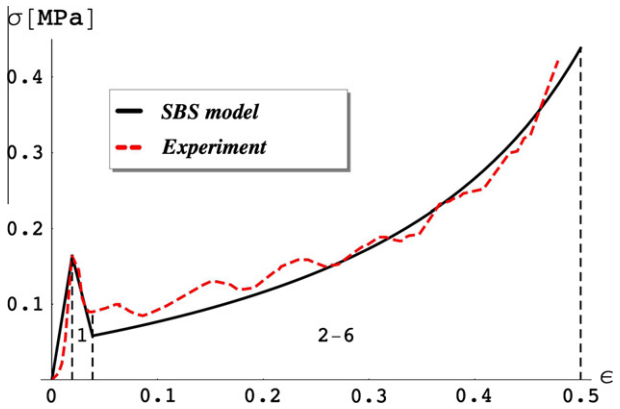

Fig. 4. Comparison between the stress–strain response of the SBS model and the experimental response (constitutive parameters in Table 1).

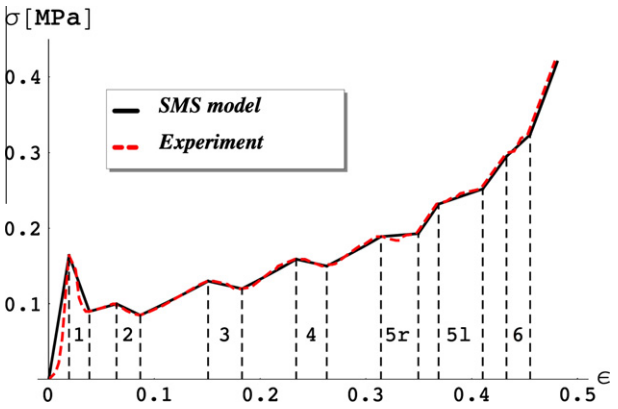

Fig. 5. Comparison between the stress–strain response of the SMS model and the experimental response (constitutive parameters in Table 2).

and the prestress σ_0 to zero, as in the previous case, we now identify the quantities $\varepsilon_a^{(i)}$, $\sigma_a^{(i)}$ with the coordinates $\bar{\varepsilon}_a^{(i)}$, $\bar{\sigma}_a^{(i)}$ of the points $\bar{P}_i^a$ of the experimental response ($i = 1,\ldots,7$), and the quantities $\varepsilon_b^{(i)}$, $\sigma_b^{(i)}$ with the coordinates $\bar{\varepsilon}_b^{(i)}$, $\bar{\sigma}_b^{(i)}$ of the points $\bar{P}_i^b$ ($i = 1,\ldots,6$). In addition, we let $\varepsilon_c^{(i)}$ and $\sigma_c^{(i)}$ coincide with $\bar{\varepsilon}_a^{(i+1)}$ and $\bar{\sigma}_a^{(i+1)}$, respectively ($i = 1,\ldots,6$). The initial stiffness k_0 of the present model is again determined through Eq. (4), as in the SBS model, while the constitutive parameters $k^{(i)}$ and $\varepsilon_*^{(i)}$ are computed by requiring that the stress–strain branches defined by Eq. (2) pass through the points $(\varepsilon_a^{(i)}, \sigma_a^{(i)})$ and $(\varepsilon_c^{(i)}, \sigma_c^{(i)})$, obtaining

$$k^{(i)} = \frac{\sigma_b^{(i)}\epsilon_c^{(i)} - \epsilon_b^{(i)}\sigma_c^{(i)} - \sigma_b^{(i)}\epsilon_b^{(i)} + \sigma_c^{(i)}\epsilon_c^{(i)} + \sigma_b^{(i)} - \sigma_c^{(i)} + \Delta}{2\left(\epsilon_b^{(i)} - \epsilon_c^{(i)}\right)} \tag{5}$$

$$\varepsilon_*^{(i)} = \frac{\sigma_b^{(i)}\epsilon_c^{(i)} - \epsilon_b^{(i)}\sigma_c^{(i)} + \sigma_b^{(i)}\epsilon_b^{(i)} - \sigma_c^{(i)}\epsilon_c^{(i)} - \sigma_b^{(i)} + \sigma_c^{(i)} + \Delta}{2\left(\sigma_b^{(i)} - \sigma_c^{(i)}\right)} \tag{6}$$

where

$$\Delta = \sqrt{\left(\sigma_c^{(i)} - \sigma_b^{(i)}\right)\left(\sigma_c^{(i)}\left(1 + \epsilon_b^{(i)} - \epsilon_c^{(i)}\right)^2 - \sigma_b^{(i)}\left(1 - \epsilon_b^{(i)} + \epsilon_c^{(i)}\right)^2\right)} \tag{7}$$

Table 2 lists the constitutive parameters that we determined for the SMS model through Eqs. (4)–(7). Fig. 5 instead shows the stress–strain response predicted by such a model, which very closely reproduces the experimentally recorded behavior. It is worth noting that the nucleation and propagation of buckles 1, 2, 3 and 4 actually leads to stress-drops and unstable stress–strain response of the pillar ($\sigma_b^{(i)} < \sigma_a^{(i)}$), while the nucleation and propagation of buckles 5 and 6 leads to stable 'bends' of the stress–strain path ($\sigma_b^{(i)} > \sigma_a^{(i)}$). This is explained by the stabilizing effect played by large material densification ($\varepsilon \geqslant 30\%$) on the stress–strain response.

Table 2
Constitutive parameters of the SMS model ($\varepsilon_0 = 0$; $\sigma_0 = 0$; initial stiffness: $k_0 = 8.357$ MPa).

Region	$\varepsilon_a^{(i)}$	$\sigma_a^{(i)}$ (MPa)	$\varepsilon_b^{(i)}$	$\sigma_b^{(i)}$ (MPa)	$k^{(i)}$ (MPa)	$\varepsilon_*^{(i)}$
1	0.019	0.164	0.038	0.090	0.132	−0.367
2	0.064	0.100	0.087	0.085	0.463	−0.069
3	0.151	0.130	0.183	0.120	0.438	−0.032
4	0.234	0.159	0.262	0.150	0.337	−0.044
5r	0.314	0.189	0.349	0.193	1.575	0.240
5l	0.369	0.232	0.410	0.252	1.313	0.249
6	0.4327	0.295	0.455	0.324	2.953	0.356

4.3. MBS model

Single spring models may be effective in the phenomenological modeling of the stress–strain response of a CNT pillar, as shown, e.g., by the SMS vs experiment comparison presented in Fig. 5. However, such models are unable to predict strain localization and multiscale effects, which may play an important role in the mechanics of CNT structures, since the latter are typically affected by multiple length- and time-scales, as we already observed in Section 1.

With the aim of developing a finer, 'microstructurally-informed' (phenomenological) modeling of the analyzed experiment (capturing the internal structure to the pillar at the micron scale), we start by observing that the analyzed experiment (as well as similar ones presented in [1]) features marked stress- and stiffness-drops in correspondence with the first buckling event, and much softer 'humps' of the stress–strain path for larger strains (cf. Fig. 2). Moving from this observation, we hereafter formulate a composite modeling of the pillar under testing, which deals with a single bistable spring turning into a collection of seven bistable springs at the end of the first buckling (FB) event (nucleation and propagation of the first buckle at the bottom of the pillar). The primary bistable spring element is introduced to account for the initial stress- and stiffness-drops of the pillar, and its response is defined by phases 0 and 1 of the SMS model presented in the previous section (cf. Table 2). Once the pillar reaches the 'post-first-buckling' (PFB) regime, such a spring splits into a chain of bistable springs piled one over the other, which aim to reproduce the buckles (or portions of buckles) forming on top of the first one, and the residual upper portion of the pillar (we assume that the first buckle is completely annihilated at the end of the FB phase). On assuming quasi-static loading conditions (i.e., discarding inertial effects), the different springs of the PFB chain carry equal axial stresses, but may feature different axial strains, due to strain localization effects (cf. also [17]). We progressively number the PFB springs from bottom-to-top, with spring i replicating the portion $p(i)$ of the pillar, where: $p(1)$, …, $p(6)$ correspond to buckles 2, 3, 4, 5r, 5l and 6, respectively, wile $p(7)$ corresponds to the portion of the pillar placed on top of the sixth buckle. It is worth noting that alternative multi-spring models of the present experiment would require chains of springs featuring at least three different stable phases. For the sake of simplicity, from now on we make use of the shorthand notations $k_0^{(i)}$, $\varepsilon_a^{(i)}$, $\varepsilon_b^{(i)}$, $\sigma_b^{(i)}$ and $k_1^{(i)}$ to denote the five independent constitutive parameters of the ith spring, letting $\sigma_a^{(i)}$ and $\varepsilon_*^{(1)}$ instead denote the corresponding dependent parameters.

As shown in [22], an effective *in situ* identification of a spring chain model requires a synced recording of the applied stress

and the axial strains of suitable vertical segments of the CNT sample under test. Once such data is available, one can draw a local stress–strain response in each analyzed segment, which is useful to identify the constitutive parameters of a single spring model representing that section of the structure. In the present case, the available SEM recording of the experiment under examination unfortunately does not help us to analytically track the local strains of the different buckles, since it is not possible to exactly locate them in the different frames of the video, and also due to a pronounced 'rocking' of the tested CNT bundle at the base, which induces coupling of axial and bending strains. Therefore, we can only roughly estimate the pre- and post-buckling strains of the different PFB springs, making use of the equations

$$\varepsilon_{a,b}^{(i)} = \frac{h^{(i)} - h_{a,b}^{(i)}}{h^{(i)}} - \varepsilon_0 \tag{8}$$

where $h_a^{(i)}$ denotes the height of the portion $p(i)$ of the bundle before collapse; $h_b^{(i)}$ denotes the corresponding height after collapse; $h^{(i)}$ indicates the undeformed height of $p(i)$; and ε_0 denotes the initial strain of the PFB system, that we set equal to the overall strain measured at the end of the FB phase ($\varepsilon_0 = \bar{\varepsilon}_b^{(1)} = 0.038$). For $i = 1, \ldots, 6$, we estimate the deformed heights $h_{a,b}^{(i)}$ through inspection of the *in situ* video, by looking at the pre- and post-collapse configurations of the different buckles, and taking the ratio between the area occupied by the generic buckle in the current frame, and the corresponding transverse dimension. Since [1] estimates the undeformed height of each buckle equal to 6 μm, and the PFB chain includes six springs modeling five different buckles (from bottom to top: buckles 2, 3, 4, 5r and 5l, and 6), we assume that each of the PFB springs approximately spans 5 μm in the unstrained configuration. Concerning the stiffness parameters, we assume $k_0^{(i)} = k_1^{(i)} = 0.537$ MPa for $i = 1, \ldots, 6$, which approximately corresponds to the average stiffness of the SMS model in the initial phase of the PFB regime (regions 2–5l, cf. Table 2). We next compute the pre- and post-buckling stresses $\sigma_{a,b}^{(i)}$ of springs 1–6, through

$$\sigma_a^{(i)} = \frac{k_0^{(i)}\varepsilon_a^{(i)}}{1-\varepsilon_a^{(i)}}, \sigma_b^{(i)} = \frac{k_0^{(i)}\varepsilon_a^{(i)}}{1-\varepsilon_a^{(i)}} - \left(\bar{\sigma}_a^{(p(i))} - \bar{\sigma}_b^{(p(i))}\right) \tag{9}$$

The identification of the constitutive parameters of springs 1–6 is completed with the determination of $\varepsilon_*^{(i)}$, which we compute as

$$\varepsilon_*^{(i)} = \varepsilon_b^{(i)} - \frac{\sigma_b^{(i)}}{k_1^{(i)} + \sigma_b^{(i)}} \tag{10}$$

For what concerns spring No. 7, we assume $k_0^{(7)} = k_1^{(7)} = 9.392$ MPa ($k_0^{(7)} \gg k_0^{(1)} = k_0^{(2)} = \cdots = k_0^{(6)}$) and absence of buckling.

The complete list of the constitutive parameters that we determined for the MBS model is given in Table 3. It is seen that the local buckling strains $\varepsilon_a^{(i)}$ progressively grow moving from spring 1 to spring 6, while the stress drops $\left(\sigma_a^{(i)} - \sigma_b^{(i)}\right)$ progressively shrink moving in the same direction. Such parameter settings allow us to mimic the effects of bottom-to-top gradients in material density

Table 3
Constitutive parameters of the MBS model in the PFB regime ($\varepsilon_0 = 0.038$; $\sigma_0 = 0.09$ MPa, $k^{(i)} = k_0^{(i)} = k_1^{(i)}$).

Spring/buckle	$\varepsilon_a^{(i)}$	$\sigma_a^{(i)}$ (MPa)	$\varepsilon_b^{(i)}$	$\sigma_b^{(i)}$ (MPa)	$k^{(i)}$ (MPa)	$\varepsilon_*^{(i)}$
1/2	0.045	0.014	0.577	−0.001	0.537	0.580
2/3	0.129	0.044	0.734	0.034	0.537	0.675
3/4	0.186	0.067	0.733	0.058	0.537	0.635
4/5r	0.229	0.088	0.664	0.108	0.537	0.497
5/5l	0.330	0.145	0.585	0.149	0.537	0.367
6/6	0.360	0.166	0.590	0.195	0.537	0.324
7/top	–	–	–	–	9.392	0.000

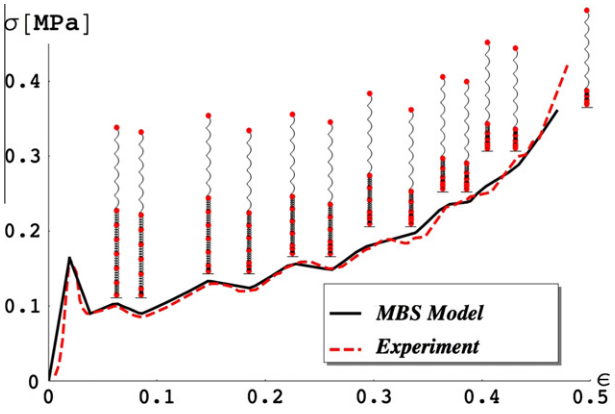

Fig. 6. Comparison between the stress–strain response of the MBS model and the experimental response (constitutive parameters in Table 3).

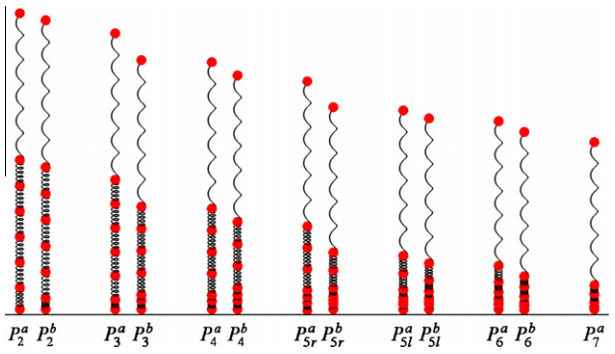

Fig. 7. Snapshots of the deformation history of the MBS model (movie animation available as Supporting online material). The snapshot $P_i^{a,b}$ simulates the configuration of the system in correspondence with point $\bar{P}_i^{a,b}$ of the experimental response.

and tubes' alignment (cf. Section 1 and Ref. [1]). The stress–strain response of the MBS model, which is provided in Fig. 6, highlights that such a model is rather effective in predicting both strain localization and the overall mechanical response of the system at hand, despite the large number of assumptions that have been introduced to identify its constitutive parameters so far. In particular, the deformation snapshots inserted into Fig. 6, which are also represented in Fig. 7 in larger scale, illustrate the ability of the MBS model in replicating the effective buckling dynamics of the examined CNT pillar in the PFB region. The discrepancies between SMS stress–strain curve and the experimental response is explained by the uncertainties related to the estimation of the local deformation histories of the different regions of the model. Such a drawback could be, e.g., overcome by marking in different colors the regions where local buckling is expected, and/or embedding strain sensors in such regions. This would allow us to *in situ* estimate all the constitutive parameters of the different sections of the model, without making any 'a priori' assumptions about local stiffness, strain and stress parameters.

5. Concluding remarks

We have presented in this work *in situ* identification procedures for multistable spring models of compressed CNT arrays, considering both single-spring and multi-spring models. The proposed procedures have been validated against a SEM-assisted compression test on a CNT bundle [1]. In the case of single-spring models, we have shown that the proposed identification procedures allow us

to accurately simulate the overall stress–strain response of the bundle, especially if a sufficiently large number of elastic phases are taken into account. Each phase reproduces the behavior of the bundle after the nucleation and (transverse) propagation of a buckle. Concerning multi-spring models, we have proved that it is possible to successfully identify the mechanical properties of a chain of multistable springs at the microscopic scale, by syncing an *in situ* SEM video recording of the bundle deformation with the stress–strain response. Such a 'microscopic' identification technique leads us to determine the local stress–strain responses of suitable vertical segments of the CNT bundle (with few micron thickness), which are in turn used to identify the constitutive parameters of a multistable spring chain model of the bundle. The latter proved to be able to effectively simulate both the overall stress–strain response, and the bottom-to-top sequential initiation and propagation of buckling folds in the bundle.

Recent studies have shown that the continuum limits of spring models (at the meso- or macro-scales) are able to capture several experimentally-observed behaviors of CNT arrays, including multiple length- and time-scale effects, bending–stretching coupling, and preconditioning damage [17,18,22,23]. The results of the present work pave the way to the effective *in situ* identification of such models, through the observation of the real stress–strain behavior of a CNT array at the microscopic scale. Without the microscale identification of multistable spring chain models, it would be required to use genetic algorithms, considering the large number of constitutive parameters involved, and the 'bumpy' nature of the fitting search space (typically featuring multiple local minima) [24–26].

Future work may lead to a refinement of the microscopic identification procedure presented in this paper, using special marking techniques of vertical segments of the CNT array, along with the formulation and experimentation of *in situ* identification techniques for 2D and 3D spatial networks of multistable springs. The latter can be used to capture the coupling of axial and bending strains, which are often observed in compression tests on CNT bundles [1] and multilayer composite materials based on CNT arrays and polymeric or metallic interlayers [22].

Acknowledgements

The authors thank Ada Amendola (Department of Civil Engineering, University of Salerno) for the support to the present work. FF acknowledges financial support from the Province of Avellino. CD acknowledges the Institute for Collaborative Biotechnologies, under Contract W911NF-09-D-0001 with the Army Research Office.

Appendix A. Supplementary material

Supplementary data associated with this article can be found, in the online version, at http://dx.doi.org/10.1016/j.compstruct.2012.09.013.

References

[1] Hutchens SB, Hall LJ, Greer JR. In situ mechanical testing reveals periodic buckle nucleation and propagation in carbon nanotube bundles. Adv Funct Mater 2010;20:2338–46.
[2] Baughman Ray H, Zakhidov Anvar A, de Heer Walt A. Carbon nanotubes – the route toward applications. Science 2002;297(5582):787–92.
[3] Andrews R, Jacques D, Rao AM, Derbyshire F, Qian D, Fan X, et al. Continuous production of aligned carbon nanotubes: a step closer to commercial realization. Chem Phys Lett 1999;303(5–6):467–74.
[4] Cao A, Dickrell PL, Sawyer WG, Ghasemi-Neihad MN, Ajayan PM. Super-compressible foam like carbon nanotube films. Science 2005;310:1307–10.
[5] Zbib AA, DjMesarovic S, Lilleodden ET, McClain D, Jiao J, Bahr DF. The coordinated buckling of carbon nanotube turfs under uniform compression. Nanotechnology 2008;19(17):175704.
[6] Raney JR, Misra A, Daraio C. Tailoring the microstructure and mechanical properties of arrays of aligned multiwall carbon nanotubes by utilizing different hydrogen concentrations during synthesis. Carbon 2011;49:3631–8.
[7] Shin MK, Oh J, Lima M, Kozlov ME, Kim SJ, Baughman RH. Elastomeric conductive composites based on carbon nanotube forests. Adv Mater 2010;22(24):2663–7.
[8] Cebeci H, de Villoria RG, Hart AJ, Wardle BL. Multifunctional properties of high volume fraction aligned carbon nanotube polymer composites with controlled morphology. Compos Sci Technol 2009;69(15–16):2649–56.
[9] García EJ, Hart AJ, Wardle BL, Slocum AH. Fabrication and nanocompression testing of aligned carbon-nanotube-polymer nanocomposites. Adv Mater 2007;19(16):2151–6.
[10] Zeng Y, Ci L, Carey BJ, Vajtai R, Ajayan PM. Design and reinforcement: vertically aligned carbon nanotube-based sandwich composites. ACS Nano 2010;4(11):6798–804.
[11] Gibson LJ, Ashby MF. Cellular solids: structure and property. 2nd ed. Oxford: Pergamon Press; 1999.
[12] Misra A, Greer JR, Daraio C. Strain rate effects in the mechanical response of polymer anchored carbon nanotube foams. Adv Mater 2009;21(3):334–8.
[13] Bradford PD, Wang X, Zhao H, Zhu YT. Tuning the compressive mechanical properties of carbon nanotube foam. Carbon 2011;49:2834–41.
[14] McCarter CM, Richards RF, Mesarovic SD, Richards CD, Bahr DF, McClain D, et al. Mechanical compliance of photolithographically defined vertically aligned carbon nanotube turf. J Mater Sci 2006;41:7872–8.
[15] Yaglioglu Onnik, Carbon nanotube based electromechanical probes. PhD thesis, Massachusetts Institute of Technology, Cambridge, Massachusetts; 2007.
[16] Yang X, He P, Gao H. Modeling frequency- and temperature-invariant dissipative behaviors of randomly entangled carbon nanotube networks under cyclic loading. Nano Res 2011;4(12):1191–8.
[17] Fraternali F, Blesgen T, Amendola A, Daraio C. Multiscale mass-spring models of carbon nanotube foams. J Mech Phys Solid 2011;59:89–102.
[18] Blesgen T, Fraternali F, Raney JR, Amendola A, Daraio C. Continuum limits of bistable spring models of carbon nanotube arrays accounting for material damage. Mech Res Commun 2012;45:58–63.
[19] Pinault M, Pichot V, Khodja H, Launois P, Reynaud C, Mayne-L'Hermite M. Evidence of sequential lift in growth of aligned multiwalled carbon nanotube multilayers. Nano Lett 2005;5(12):2394–8.
[20] Pathak S, Lim EJ, Abadi PPSS, Graham S, Cola BA, Greer JR. Higher recovery and better energy dissipation at faster strain rates in carbon nanotube bundles: an in situ study. ACS Nano 2012;6(3):2189–97.
[21] Puglisi G, Truskinovsky L. Thermodynamics of rate-independent plasticity. J Mech Phys Solids 2005;53(3):655–79.
[22] Raney JR, Fraternali F, Amendola A, Daraio C. Modeling and in situ identification of material parameters for layered structures based on carbon nanotube arrays. Compos Struct 2011;93:3013–8.
[23] Schmidt B, Fraternali F. Universal formulae for the limiting elastic energy of membrane networks. J Mech Phys Solid 2012;60:172–80.
[24] Fraternali F, Porter MA, Daraio C. Optimal design of composite granular protectors. Mech Adv Mater Struct 2010;17:1–19.
[25] Elsayed T, Mota A, Fraternali F, Ortiz M. A variational constitutive model for soft biological tissues. J Biomech 2008;41:1458–66.
[26] Fraternali F, Marino A, Elsayed T, Della Cioppa A. Structural shape optimization via variational methods and evolutionary algorithms. Mech Adv Mater Struct 2011;18:225–43.